

## **Sub-wavelength patterning of organic monolayers via nonlinear processing with continuous-wave lasers**

Mathieu, Mareike; Hartmann, Nils

This text is provided by DuEPublico, the central repository of the University Duisburg-Essen.

This version of the e-publication may differ from a potential published print or online version.

DOI: <https://doi.org/10.1088/1367-2630/12/12/125017>

URN: <urn:nbn:de:hbz:464-20180814-152943-3>

Link: <https://duepublico.uni-duisburg-essen.de:443/servlets/DocumentServlet?id=46727>

Legal notice:

© IOP Publishing Ltd and Deutsche Physikalische Gesellschaft.

NJP copyright statement:

The content in IOP's journals and those published on behalf of their partners is protected by copyright.

Articles submitted prior to November 2012: [Creative Commons Attribution-NonCommercial-ShareAlike 3.0 Unported](#)

Source: New Journal of Physics 12 (2010) 125017; published 22 December 2010

## Sub-wavelength patterning of organic monolayers via nonlinear processing with continuous-wave lasers

Mareike Mathieu and Nils Hartmann<sup>1</sup>

Fakultät für Chemie, Universität Duisburg-Essen, 45117 Essen, Germany  
CeNIDE—Center for Nanointegration Duisburg-Essen, 47048 Duisburg,  
Germany

NETZ—NanoEnergieTechnikZentrum, 47048 Duisburg, Germany

E-mail: [nils.hartmann@uni-due.de](mailto:nils.hartmann@uni-due.de)

*New Journal of Physics* **12** (2010) 125017 (21pp)

Received 14 April 2010

Published 22 December 2010

Online at <http://www.njp.org/>

doi:10.1088/1367-2630/12/12/125017

**Abstract.** In recent years, nonlinear processing with continuous-wave lasers has been demonstrated to be a facile means of rapid nanopatterning of organic monolayers down to the sub-100 nm range. In this study, we report on laser patterning of thiol-based organic monolayers with sub-wavelength resolution. Au-coated silicon substrates are functionalized with 1-hexadecanethiol. Irradiation with a focused beam of an Ar<sup>+</sup> laser operating at  $\lambda = 514$  nm allows one to locally remove the monolayer. Subsequently, the patterns are transferred into the Au film via selective etching in a ferri-/ferrocyanide solution. Despite a  $1/e^2$  spot diameter of about  $2.8 \mu\text{m}$ , structures with lateral dimensions down to 250 nm are fabricated. The underlying nonlinear dependence of the patterning process on laser intensity is traced back to the interplay between the laser-induced transient local temperature rise and the thermally activated desorption of the thiol molecules. A simple thermokinetic analysis of the data allows us to determine the effective kinetic parameters. These results complement our previous work on photothermal laser patterning of ultrathin organic coatings, such as silane-based organic monolayers, organo/silicon interfaces and supported membranes. A general introduction to nonlinear laser processing of organic monolayers is presented.

<sup>1</sup> Author to whom any correspondence should be addressed.

**Contents**

<b>1. Introduction</b>	<b>2</b>
1.1. General concepts in micro- and nanofabrication . . . . .	2
1.2. Self-assembled organic monolayers . . . . .	3
1.3. Patterning of self-assembled monolayers . . . . .	4
1.4. Nonlinear laser processing of self-assembled monolayers . . . . .	5
<b>2. Experimental</b>	<b>7</b>
<b>3. Alkanethiol monolayers</b>	<b>10</b>
3.1. Photothermal laser processing . . . . .	10
3.2. Thermokinetic analysis . . . . .	12
3.3. Discussion and comparison . . . . .	16
<b>4. Conclusions and perspectives</b>	<b>18</b>
<b>Acknowledgments</b>	<b>19</b>
<b>References</b>	<b>19</b>

**1. Introduction***1.1. General concepts in micro- and nanofabrication*

Progress in micro- and nanopatterning is key to the development of novel components and devices in the present and emerging technologies [1]–[3]. Biochemical patterning techniques, for example, have been demonstrated to allow for the integration of neurons in microchip structures [4, 5]. Photonic crystals, as another example, provide promising perspectives in engineering sensor devices with enhanced sensitivities [6, 7]. These examples illuminate just a few innovative directions in microfabrication. In view of the ongoing miniaturization in the semiconductor industry and other technological areas, and the fascinating opportunities that are within reach in nanotechnology, most studies in this field, of course, focus on nanofabrication [1]–[3]. Here, generally, two avenues are distinguished. On the one hand, following the top-down approach, advanced lithographic techniques are employed in order to fabricate increasingly smaller structures [8]–[10]. On the other hand, inspired by nature, in the bottom-up approach the synthesis of increasingly larger structures via self-assembly and self-organization of molecular components and nanoscopic building blocks is targeted [10]–[13].

Both avenues encounter significant challenges at length scales between 1 and 100 nm [10]. On the one hand, a variety of nanolithographic techniques allow for the fabrication of structures with lateral dimensions well below 10 nm [14, 15]. The throughput of these techniques, however, is very low and hence large-area patterning is not feasible. On the other hand, modern techniques in chemical synthesis provide the basis for a broad range of nanoscopic building blocks with predefined size, structure and function, e.g. supramolecular receptors, block copolymers, nanoparticles and nanowires [11]–[13]. These components can also be assembled on surfaces in highly ordered arrangements [16]–[18]. The fabrication of functional device structures, however, usually necessitates large-scale integration into arrangements that vary over several length scales in order to connect these components to each other and to the macroscopic world. To what extent such complex structures some day can be fabricated, as in nature, solely via self-assembly and self-organization is not foreseeable today. In the

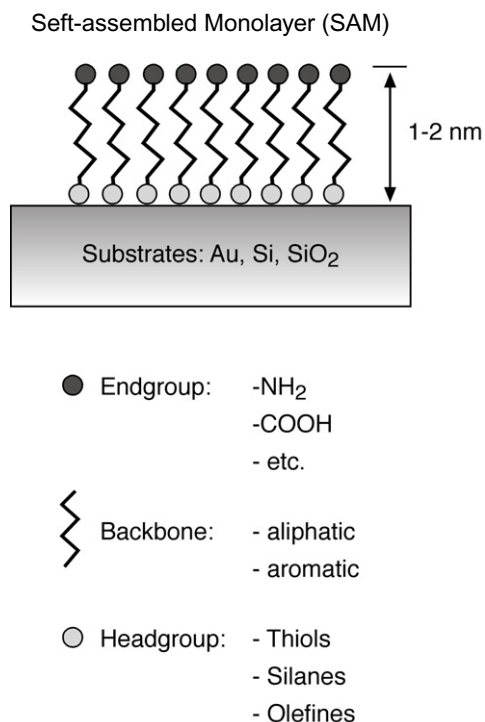


**Figure 1.** Schematic diagram of the structure of SAMs. Three functional parts of the adsorbed molecules are distinguished: the head group, the backbone and the end group.

meantime, however, it is generally accepted that progress in the near future could well benefit from some fundamental principles that are exploited in nature [10]. One of those principles is the directed self-assembly of nanoscopic building blocks on chemical templates. A prominent example in nature can be found at the very bottom of life, namely in DNA replication. Here, a single DNA strand represents a linear template onto which complementary nucleotides are assembled in order to build up a new DNA strand. A common approach in nanofabrication that takes advantage of this principle considers the fabrication of nanostructured chemical templates on flat solid platforms [19]. These templates expose functional domains that allow one to selectively couple complementarily functionalized components, such as nanoparticles, polymers and biomolecules [19]–[23].

### 1.2. Self-assembled organic monolayers

Flat platforms are a simple basic requirement in order to ensure precise vertical alignment of the components and allow for building up complex architectures, i.e. multilevel structures from distinct components [24]–[26]. In addition, of course, the fabrication of chemical templates necessitates suitable functionalization and patterning routines [19]–[23]. Here, self-assembled organic monolayers (SAMs) have evolved as a particularly versatile means, cf figure 1 [27]–[30]. Generally, these ultrathin films consist of densely packed elongated molecules, which stand upright or nearly upright on top of the substrate's surface. Each molecule can be divided into three functional parts: (i) the head group, which couples the molecules to the surface and defines the type of SAM. Most prominent are thiol-based SAMs on gold and

other coinage metals [28], silane-based SAMs on oxidic or surface-oxidized substrates [29] and organic monolayers from olefinic precursor molecules on semiconducting platforms [30]; (ii) the backbone, which in the simplest case represents an aliphatic hydrocarbon chain; and (iii) the end group, e.g. simple functional groups such as amine or carboxyl groups or more complex chemical or biochemical functionalities [32, 33]. Upon choosing the end group, a variety of surface properties, such as wettability, biocompatibility and chemical reactivity and resistance, can be tailored. In conjunction with patterning routines this provides a facile means to fabricate flat chemical templates with domains of defined size, shape and chemical termination [19].

### 1.3. Patterning of self-assembled monolayers

A common approach toward patterned SAMs considers the application of lithographic techniques [28]–[31]. For this purpose, a broad range of distinct techniques can be used including photolithography [28]–[31], micro contact printing ( $\mu$ CP) [34], electron beam lithography [35] and various scanning probe techniques, such as scanning near-field lithography and dip-pen nanolithography [36]–[39]. Each technique comes with a particular set of features, which makes it useful or superior for certain applications and less suitable or simply unfeasible for others. Hence, even if there are numerous patterning techniques available today, there simply is no ultimate tool that covers all the needs in micro- and nanofabrication. This drives the ongoing efforts in several groups around the world to advance, present and explore new patterning procedures.

Generally, parallel and sequential patterning techniques can be distinguished [1]–[3]. Parallel techniques, such as photolithography and  $\mu$ CP, allow for fast simultaneous patterning of large areas using a mask or master of the desired pattern. For this reason, parallel techniques are most efficient for mass fabrication of identical copies. Most prominent is the fabrication of microchips in the semiconductor industry [10]. Mask fabrication, however, is time-consuming and cost-intensive and, hence, parallel techniques are not suitable for applications where the pattern design frequently changes, e.g. in rapid prototyping and small-volume fabrication. In contrast, sequential techniques, such as electron beam lithography and scanning probe techniques, require no mask or master. In particular, patterning is carried out in a serial manner via direct writing of structures. Hence, such techniques, in general, are comparatively slow and not suitable for rapid large-area patterning, but are particularly useful in fundamental scientific studies and in designing and changing single copies, e.g. in mask fabrication and mask repair.

Among the key features that are commonly used to characterize a given patterning technique, be it parallel or sequential, the achievable lateral resolution, of course, is of particular importance. With regard to technical applications, the photolithographic process used in microchip fabrication in this respect represents a remarkable benchmark. Feature sizes on current microchips already are far below 100 nm. Investment and operating costs, however, are enormous and keep rising. In addition, the whole process flow, of course, is adapted to the geometric constraints and specific materials considered in microchip fabrication. This limits the wider use of photolithography at this level of perfection. Hence, with the ongoing miniaturization in a variety of technological applications beyond microchip fabrication, there is an increasing demand for cost-effective, flexible techniques that allow for rapid large-area micro- and nanofabrication [40]. Here laser direct processing techniques provide some particularly promising perspectives [40]–[44].

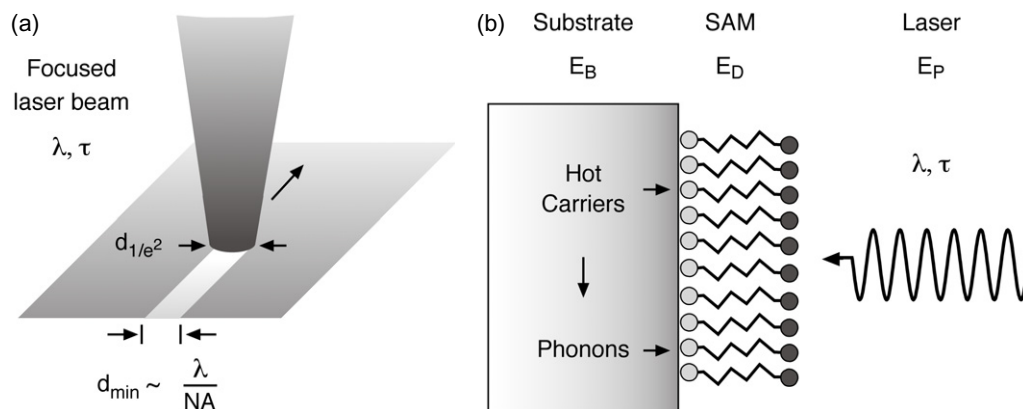


**Figure 2.** Direct laser processing of organic monolayers: (a) patterning principle and (b) energetic constraints and photoexcited processes. Notations in (a) and (b) are laser wavelength  $\lambda$ , laser pulse length  $\tau$ ,  $1/e^2$  laser spot size  $d_{1/e^2}$ , minimum structure size  $d_{\min}$ , numerical aperture of the focusing optics NA, photon energy  $E_P$ , linear photodissociation threshold of the organic monolayer  $E_D$  and band gap  $E_B$  of the substrate.

#### 1.4. Nonlinear laser processing of self-assembled monolayers

Direct laser processing of SAMs, which is addressed in this paper, appears promising because of a variety of general features as outlined in the following [45]–[64]. On the one hand, the ultrathin nature of these coatings ensures short processing times and provides the basis for well-defined irradiation along the optical axis [28, 29]. It also allows for burr-free patterning and avoids bubble and particle formation, all of which are common problems in ablative laser patterning techniques [41, 65]. In addition, varying the chemical structure of the monolayers provides a way to tailor sensitivity and resist properties and opens up an avenue toward chemical patterning [28, 29]. On the other hand, laser processing is a sequential noncontact technique, which requires no resist or mask and offers a particularly high flexibility in two dimensions (2D) and three dimensions (3D) [40, 41, 66]. Moreover, processing can be carried out at high pressures or in liquids, and on—or even in—dielectric materials and patterning is feasible at fast writing speeds over wafer scale areas. This set of features distinguishes laser direct patterning techniques from all other lithographic techniques and explains its widespread use in many technical applications including optical data storage and optical engineering [43, 67].

If nanopatterning of organic monolayers is targeted, the optical diffraction limit, of course, poses a significant constraint, cf figure 2(a). Even if highly focusing optics with a numerical aperture (NA) close to one is used, the structure sizes usually are not much smaller than the wavelength of the laser light [41]. A common means of extending the lateral resolution of laser techniques into the sub-wavelength range takes advantage of nonlinear effects [41]–[44].

If one considers the complexity of photoexcited processes at surfaces, the pool of nonlinearities, of course, is large [68]–[70]. In general, direct and indirect excitation mechanisms can be distinguished, cf figure 2(b). Direct mechanisms are based on an immediate excitation of the adsorbed molecules within the monolayer. Examples include photoexcitation via single or multiphoton processes and field-induced processes. In contrast, indirect mechanisms start with excitation processes that are initiated in the substrate. Absorption

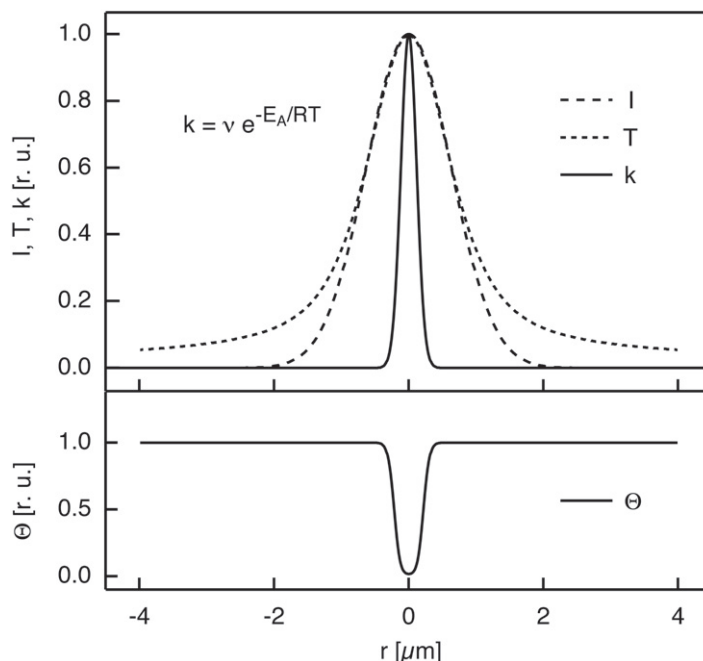


**Figure 3.** Schematic diagram of the photothermal effect in nonlinear processing of organic monolayers with continuous-wave lasers. Profiles of the laser intensity  $I$ , the surface temperature  $T$ , the reaction rate constant  $k$  and the surface coverage  $\theta$ . The Arrhenius equation given at the top left introduces a strong nonlinearity. Notations are: frequency factor  $\nu$ , activation energy  $E_A$ , ideal gas constant  $R$ , radial distance  $r$ .

of laser light in the substrate at first generates excited charge carriers, such as hot electrons. On the one hand, these electrons may interact with the adsorbed molecules building up the monolayer and initiate reactions. Examples are photochemical or photoelectrochemical reaction pathways. On the other hand, the excited electrons eventually scatter inelastically with the substrate lattice, which inevitably results in a certain temperature rise at the surface. This provides the basis for photothermal reaction pathways.

All the aforementioned processes proceed on material-specific time, length and energy scales, which vary over several orders of magnitude. This makes laser patterning a rich and complex process [41]. For this reason, nonlinear laser processing of organic monolayers, at first, necessitates a proper choice of all laser parameters in order to trigger the desired surface reactions and avoid damage of the substrate. Figure 2(b) depicts some of the essential energetic parameters: the photon energy  $E_P$ , the linear photodissociation threshold  $E_D$  of the monolayer and, if applicable, the band gap  $E_B$  of the substrate. Commonly, in nonlinear laser processing, photon energies well below the photodissociation threshold are chosen [45]–[54]. This allows for sub-wavelength patterning [45, 52]. Femtosecond lasers provide promising perspectives in sub-wavelength patterning via multiphoton absorption processes [45, 46]. Continuous-wave lasers, in turn, have been demonstrated to be a powerful tool for sub-wavelength patterning of organic monolayers exploiting photothermal processes [50]. In photothermal processing, a focused laser beam is used to locally heat the substrate surface and to thermally initiate chemical reactions [41]. As depicted in figure 3, the corresponding temperature profile  $T$

usually closely follows the laser intensity profile  $I$ . The temperature dependence of the reaction via the Arrhenius equation, however, introduces a strong nonlinearity. In particular, because of the activated decomposition process, the lateral variation of the rate constant  $k$  and the surface coverage  $\theta$  can be very narrow. At short irradiation times, decomposition remains confined to a small area at the center of the laser spot where high temperatures and, hence, high reaction rates are reached. At high activation energies  $E_A$ , photothermal processing allows for sub-wavelength patterning even though the laser spot exhibits a width of a few microns. For this reason, strongly bound coatings, such as silane-based SAMs, are most effective in photothermal processing [50]–[53]. Alkylsiloxane monolayers, for example, exhibit exceptionally high thermal and chemical and photochemical stability [29]. Hence, structures with lateral dimensions well below 100 nm can be fabricated [52]. In conjunction with chemical functionalization routines, this provides an avenue toward nanostructured chemical templates for the directed self-assembly of nanoparticles, polymers and other components, as shown in figure 4 [52, 53]. These results emphasize the capabilities of photothermal procedures in nanofabrication of silane-based chemical templates. Photothermal processing, however, is not limited to silane-based SAMs, but can be used for nanopatterning of organo/silicon interfaces [54], thiol-based SAMs [55]–[58] and non-covalently bound soft coatings, such as supported phospholipid membranes [59]. Further studies also considered various constructive schemes for chemical micro- and nanopatterning of organic and inorganic interfaces [60]–[63]. Moreover, parallel processing has been demonstrated using micro-lens arrays and interference patterns [71, 72].

In this paper, photothermal processing of alkanethiol SAMs is addressed. Previous studies by Amirfazli and co-workers have already demonstrated the versatility of this approach in micropatterning of thiol-based SAMs [55, 56]. Using highly focusing immersion optics, recently sub-micron structures have also been fabricated [58]. Patterning in this study, however, has been carried out at fairly long exposure times of a few minutes, where the processing is linear in the applied laser power density. Hence, the minimum structure size was almost equal to the laser spot size and the optics essentially left no room for further improvement. Here, we explore the capabilities of nonlinear photothermal laser processing in nanopatterning of these coatings at exposure times in the milli- and microsecond regime. This opens up an avenue toward rapid fabrication of structures with lateral dimensions below 100 nm.

## 2. Experimental

A schematic drawing of the process flow is shown in figure 5. Commercial Si(100) wafers coated with a 5 nm Ti adhesion layer and a 40 nm Au layer (Mateck) are cut into small pieces, about  $10 \times 10 \text{ mm}^2$  in size, and used as substrates. For coating with alkanethiol monolayers, all samples are first cleaned with hot piranha solution (3 : 1 mixture of 96% sulfuric acid and 30% hydrogen peroxide) for 5 min, thoroughly rinsed in ultrapure water and dried in a stream of high-purity argon. Subsequently, these samples are immersed in a 1 mM solution of 1-hexadecanethiol (HDT; Fluka) in degassed ethanol in a glove box for 18 h, followed by rinsing in ethanol and drying with argon. Static water contact angle measurements on such samples yield values around  $109^\circ$ . All subsequent experiments are carried out immediately after coating.

Photothermal patterning is performed under ambient conditions, that is, in ambient air at room temperature, with an experimental setup as depicted in figure 6. Briefly, the beam of an  $\text{Ar}^+$  laser operating at  $\lambda = 514 \text{ nm}$  is focused onto the sample surface using a beam

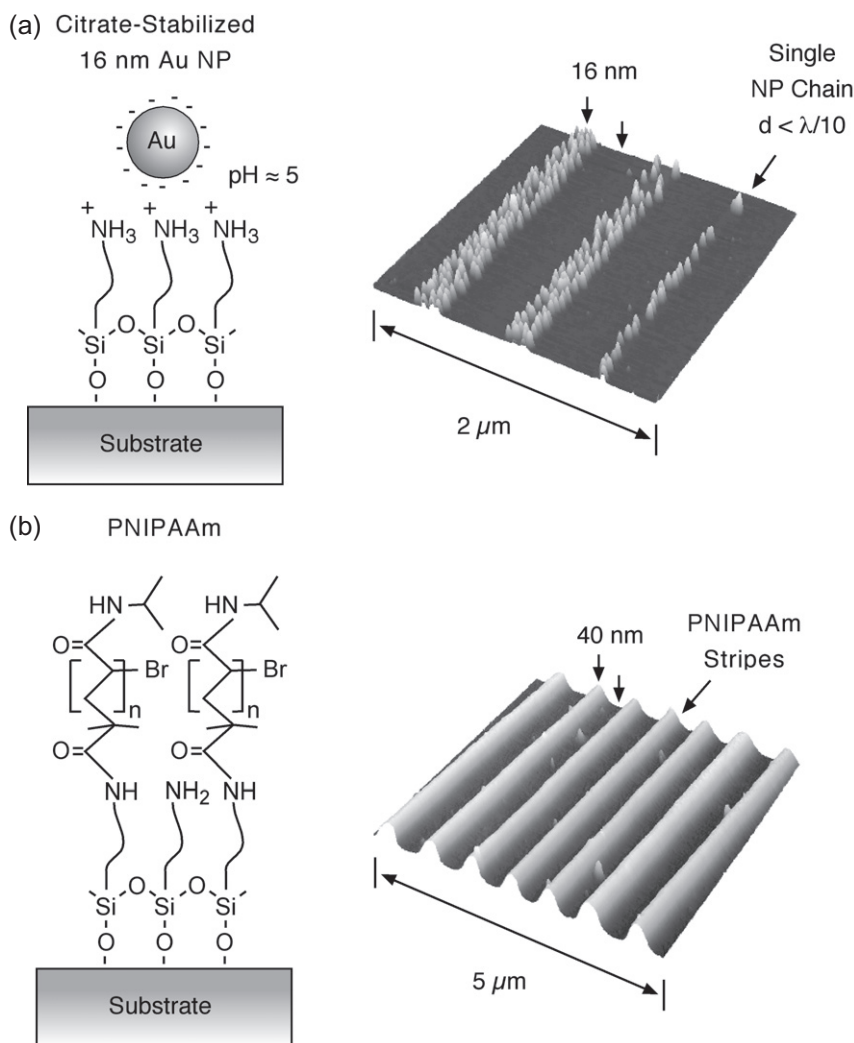


**Figure 4.** Directed self-assembly on nanostructured chemical templates. (a) Selective adsorption of citrate-stabilized 16 nm Au nanoparticles. (b) Surface-initiated polymerization of poly(*N*-isopropylacrylamide). The templates have been fabricated via photothermal processing of silane-based monolayers on SiO<sub>2</sub>/Si at a wavelength of  $\lambda = 514$  nm and a  $1/e^2$  laser spot size  $d_{1/e^2} \approx 2.5$   $\mu\text{m}$  followed by post-functionalization, yielding aminated organic surface stripes with widths down to 100 nm and below. As shown in (a), on such stripes single chains of Au nanoparticles are formed. These gold structures exhibit a width of less than  $\lambda/10$ . For further details, cf [52] and [53].

expander and a microscope objective with an NA of 0.25. Laser beam profiling with a knife-edge system (Beam Master BM-3 UV-VIS, Coherent) reveals a Gaussian beam shape with a  $1/e^2$  focal spot diameter of  $2.8 \pm 0.3$   $\mu\text{m}$ . For positioning, the objective is mounted on a high-resolution stepper motor stage. Two equivalent stepper motor stages are used to translate the sample surface in the focal plane of the objective. Processing with this setup is feasible over an area of  $25 \times 25$  mm<sup>2</sup>. For sample alignment purposes the back-reflected laser light is projected onto a screen. Generally, patterning can be carried out either in continuous-mode operation

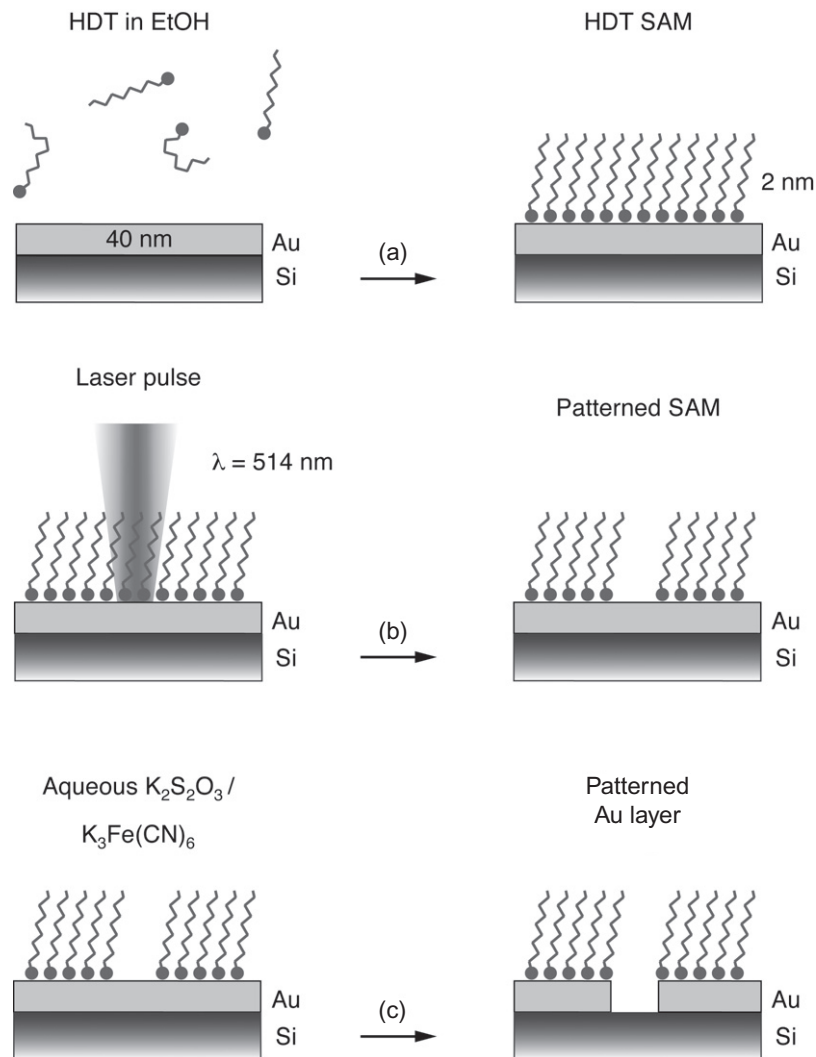


**Figure 5.** Schematic diagram of the process flow: (a) SAM formation upon immersion in an ethanolic solution of HDT, (b) photothermal laser processing of the HDT SAM at  $\lambda = 514$  nm and (c) pattern transfer into the Au film upon etching in an aqueous solution of  $K_2S_2O_8$  and  $K_3Fe(CN)_6$ .

or in pulse-mode operation [54]. In continuous-mode operation, the laser spot is moved along lines at a writing speed of up to  $25 \text{ mm s}^{-1}$ . In pulse-mode operation, an acousto-optical tunable filter (AOTF) is used to chop the laser beam at a fixed position and generate laser pulses in the range of micro- to milliseconds. Rising and falling times of the AOTF are below  $5 \mu\text{s}$ . The AOTF also allows for adjustment of the laser power, both in continuous-mode and pulse-mode operation. Common patterning parameters in continuous-mode operation are the incident laser power  $P$  and the writing speed  $v$ . Common patterning parameters in pulse-mode operation are the incident laser power  $P$  and the pulse length  $\tau$ . The laser power  $P$  on the samples is measured using a commercial power meter with a thermal sensor (LM-10/Field Master GS, Coherent). For monitoring during patterning, a few per cent of the laser light is directed into the power meter.

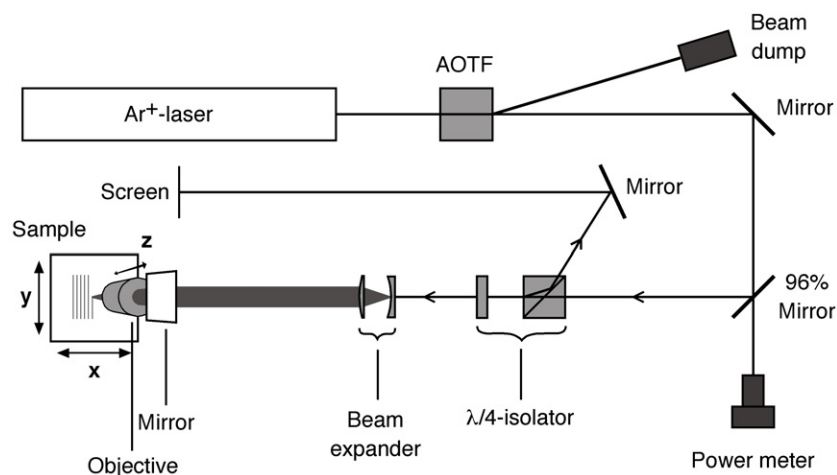


**Figure 6.** Schematic diagram of the experimental setup for photothermal laser patterning.

For characterization, the patterns are transferred into the Au film via selective etching [73]. For this purpose, the patterned samples are immersed in a solution of  $\text{K}_2\text{S}_2\text{O}_3$  (0.1 M), KOH (1.0 M),  $\text{K}_3\text{Fe}(\text{CN})_6$  (0.01 M), and  $\text{K}_4\text{Fe}(\text{CN})_6$  (0.001 M) at room temperature for 16–18 min. This immersion time suffices to completely dissolve the Au film in laser-depleted surface areas, whereas widening of the structures because of the isotropic etching process remains minimal. After etching, the samples are rinsed in ultrapure water and blown dry with argon.

Atomic force microscopy (AFM; Autoprobe CP from Veeco) is used for characterization. AFM images are recorded in contact mode with standard cantilevers. Width measurements are not corrected for tip size effects and refer to values measured at half-depth.

### 3. Alkanethiol monolayers

#### 3.1. Photothermal laser processing

Photochemical patterning of alkanethiol monolayers is usually carried out at wavelengths in the deep ultraviolet regime [28, 74]. In contrast, laser processing of HDT monolayers in this study is performed at  $\lambda = 514$  nm. At this wavelength the monolayer is highly transparent. Hence, processing is expected to proceed via indirect, substrate-mediated, mechanisms, cf figure 2(b). Considering the  $1/e$  penetration depths at  $\lambda = 514$  nm of 22 nm [75], laser light absorption essentially takes place in the Au film, where photo-excited carriers rapidly scatter with the substrate lattice and generate heat. Because of the local temperature rise, thermal desorption of the monolayer is initiated [55, 56].

Commonly, laser direct patterning is carried out in continuous-mode operation [50]–[56]. This allows for the fabrication of line patterns. In the study presented here, the laser power  $P$  and writing speed  $v$  have been varied between 160 and 290 mW and 0.5 and 25  $\text{mm s}^{-1}$ , respectively. Typical AFM data are shown in figure 7. The line pattern is clearly visible both in the topographic image and in the friction image. Line depths are about 1–2 nm, which is equivalent to the thickness of HDT monolayers on Au [27, 28]. In particular, laser irradiation allows one to remove the organic monolayer. Moreover, in the parameter range considered

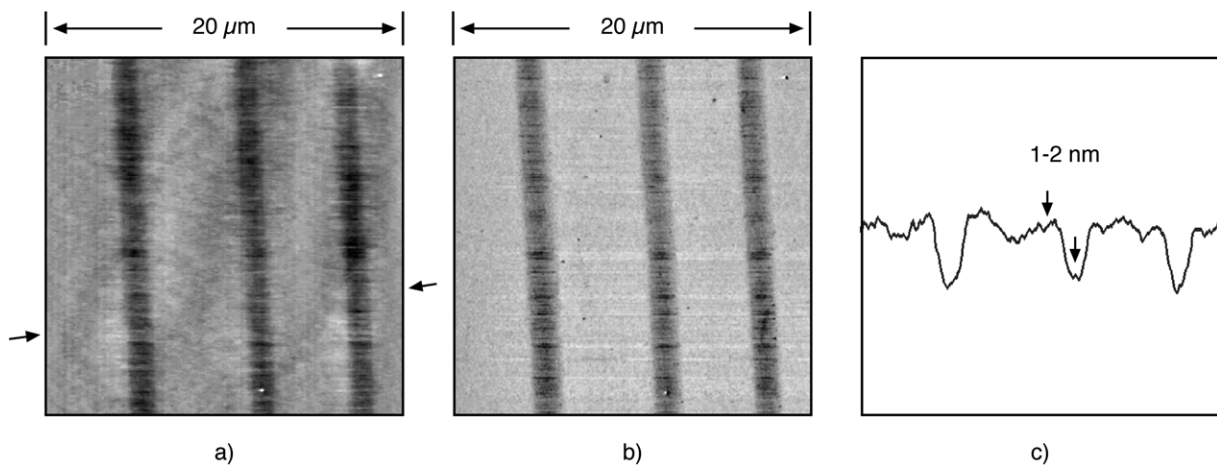


**Figure 7.** AFM data from patterning experiments of HDT SAMs on Au-coated silicon samples in continuous-mode operation at  $\lambda = 514$  nm,  $d_{1/e^2} = 2.8$   $\mu\text{m}$ ,  $P = 290$  mW and distinct  $v = 2, 5$  and  $10$   $\text{mm s}^{-1}$ : (a) topography, (b) friction contrast and (c) averaged height profile at the position indicated by black arrows in (a).

here, no variation of the line depths is observed, suggesting that thermal desorption of the thiol molecules is highly selective [58].

In order to determine the dependence of the structure size on the laser parameters, processing of HDT monolayers is carried out in pulse-mode operation. In this mode, the respective rising and falling times during irradiation are a few microseconds only. This ensures well-defined irradiation time and temperature rise and hence provides the basis for a detailed analysis of the data [54]. Laser power  $P$  and pulse length  $\tau$  are varied between 160 and 280 mW and between 50  $\mu\text{s}$  and 50 ms, respectively. For AFM measurements the patterns are transferred into the Au film by selective etching in a ferri-/ferrocyanide solution [73]. This results in an increased topography and hence allows for convenient characterization of the structures. Figure 8 displays a topographic AFM image and a corresponding height profile of structures that are transferred into the Au film following this procedure. Evidently, etching completely dissolves the Au film at the center of the irradiated spots reaching a depth of about 40 nm, whereas the organic coating inhibits etching in the surrounding areas. Note that no defect formation is observed in the surrounding areas, suggesting that these areas are covered with a densely packed monolayer. It is worth noting that the widths of the structures, as measured at half-depth,  $d_{1/2} = 870$  and 460 nm, respectively, are significantly smaller than the  $1/e^2$  laser spot diameter of 2.8  $\mu\text{m}$ , indicating a highly nonlinear dependence of the overall patterning process on the incident laser power. Figure 9 shows the patterns that have been fabricated at laser powers of 274 and 198 mW, respectively, and pulse lengths between 50  $\mu\text{s}$  and 50 ms. Note that during laser processing, positions along the diagonal from the top left to the bottom right were skipped intentionally in order to allow for easy reference to the laser parameters. A diagram of the structure diameters for various laser powers and pulse lengths is displayed in figure 10(a). Generally, the diameter decreases with decreasing laser power and pulse length. Diameters at high laser powers and long pulse lengths are about 2.4  $\mu\text{m}$ , i.e. almost equal to the laser spot size. In contrast, at low laser powers and short pulse length, the diameters are much

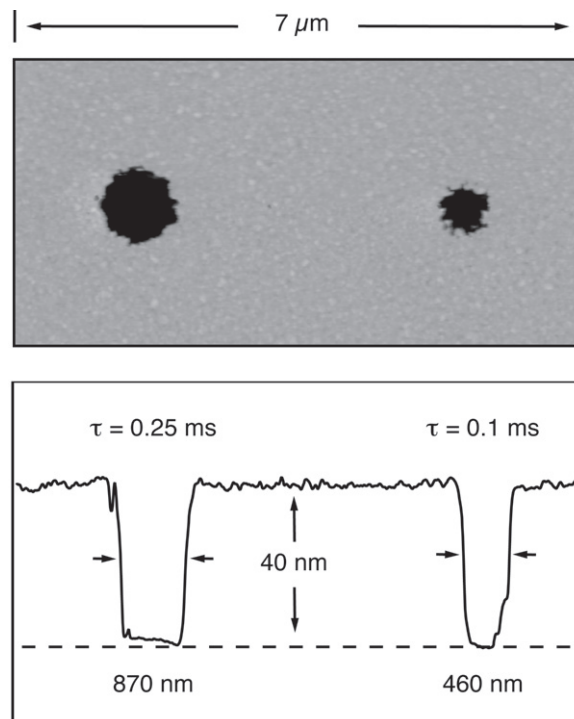


**Figure 8.** AFM data from patterning experiments of HDT SAMs on Au-coated silicon samples in pulse-mode operation with single laser pulses at  $\lambda = 514$  nm,  $d_{1/e^2} = 2.8 \mu\text{m}$ ,  $P = 218$  mW and distinct  $\tau$  as depicted in the height profile. After laser processing the patterns are transferred into the Au film via wet etching. The dashed line in the height profile marks the position of the silicon substrate level. Given diameters refer to values at half-depth.

smaller than the laser spot diameter. At these parameters minimum structure sizes are below 300 nm, that is, sub-wavelength patterning is feasible, cf figure 10(b). Note that these structures exhibit a depth of 40 nm, that is, the gold at the center is completely dissolved. The diameters, however, vary somewhat. Average values are about 230 nm. Processing at lower laser powers and shorter pulse lengths, in turn, does not yield any structures.

### 3.2. Thermokinetic analysis

For thermokinetic analysis of the data, we here closely follow a procedure as reported in previous contributions [50, 54]. In particular, for each data point in figure 10(a), the half-life reaction time  $\tau_{1/2}$  of the initiated desorption process and the respective temperature rise  $T$  at the structure edge during irradiation are considered, as depicted in figure 11(a). This analysis, in general, is in close analogy to common laser-induced thermal desorption (LITD) studies [76]–[79]. Whereas in LITD, however, usually desorption spectra are analyzed, in the following, spatial profiles of surface structures are considered.  $\tau_{1/2}$  and  $T$  are correlated via [54]

$$\tau_{1/2} = A \exp(E_A/RT), \quad (1a)$$

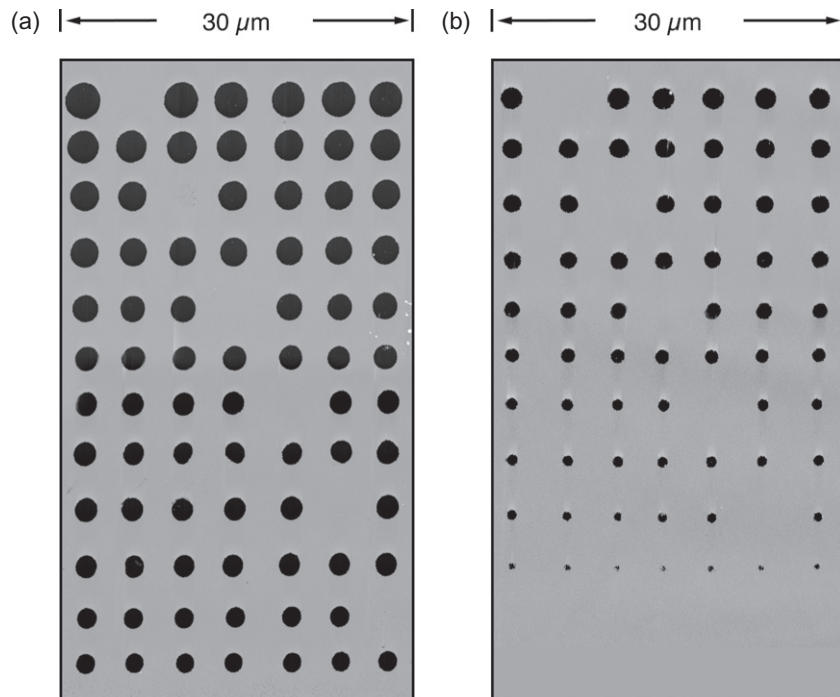


**Figure 9.** AFM images of laser-fabricated hole patterns. HDT SAMs on Au-coated silicon samples are processed in pulse-mode operation with single laser pulses at  $\lambda = 514 \text{ nm}$ ,  $d_{1/e^2} = 2.8 \mu\text{m}$ , (a)  $P = 274 \text{ mW}$ , (b)  $P = 198 \text{ mW}$  and distinct  $\tau$  between  $50 \mu\text{s}$  (bottom rows) and  $50 \text{ ms}$  (top rows). For pattern transfer the samples are wet-chemically etched. Note that, during laser processing, positions along the diagonal from the top left to the bottom right were skipped intentionally in order to allow for easy reference to the laser parameters.

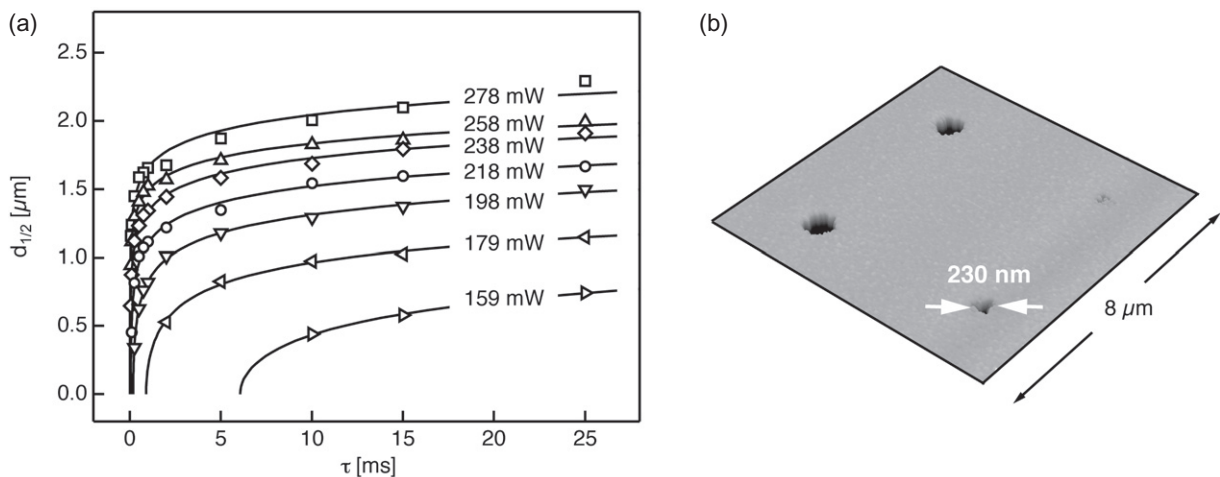


**Figure 10.** (a) Dependence of the structure diameter  $d_{1/2}$  at half-depth on the incident laser power  $P$  and the pulse length  $\tau$ . Processing is carried out at  $\lambda = 514 \text{ nm}$ ,  $d_{1/e^2} = 2.8 \mu\text{m}$ . The lines are only a guide to the eyes. (b) 3D presentation of small structures after laser processing at  $P = 198 \text{ mW}$  and  $\tau = 0.5 \text{ ms}$  (top row) and  $\tau = 0.25 \text{ ms}$  (bottom row).

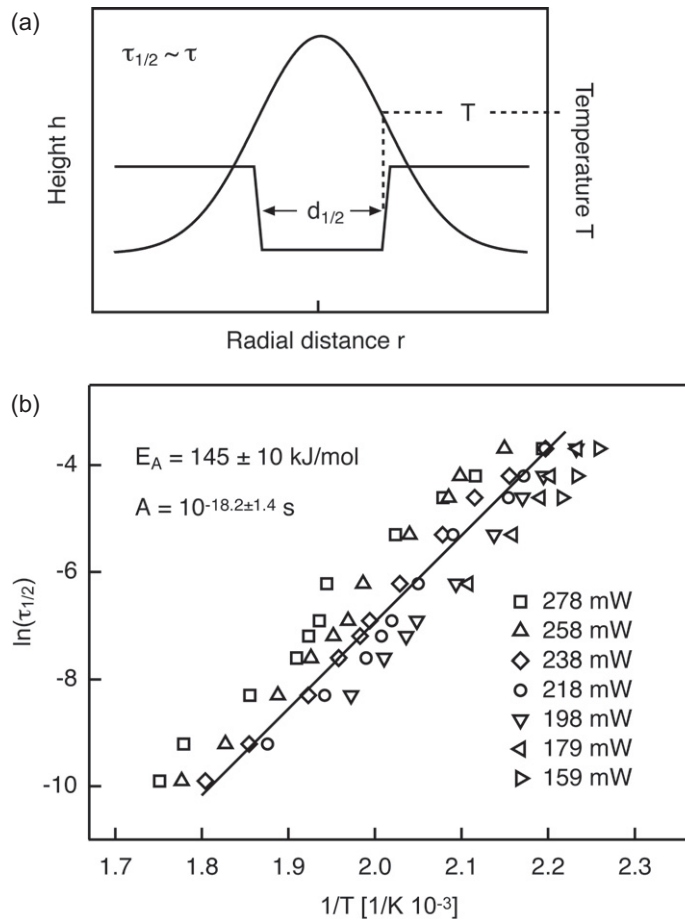


**Figure 11.** (a) Schematic diagram depicting the assignment of the temperature  $T$  at the structure edge and the corresponding half-life time  $\tau_{1/2}$  used in thermokinetic analysis of the data in figure 10(a). For each data point,  $T$  is calculated on the basis of equations (2a) and (2b).  $\tau_{1/2}$ , in turn, scales with the laser pulse length  $\tau$ . (b) Arrhenius-type diagram of the data in figure 10(a) on the basis of equation (1a).  $T$  and  $\tau_{1/2}$  are determined as depicted in figure 11(a).

where the prefactor  $A$  and the activation energy  $E_A$  represent the effective kinetic parameters of the initiated process and  $R$  refers to the ideal gas constant. For comparison, in the Arrhenius equation the corresponding reaction rate constant  $k$  is considered:

$$k = \nu \exp(-E_A/RT), \quad (1b)$$

where  $\nu$  is the respective frequency factor.  $\nu$  and  $A$  are inversely proportional [80]. For a first-order reaction  $\nu = \ln 2/A$ . For a second-order reaction  $\nu = 1/A\theta_0$ , where  $\theta_0$  denotes the initial surface coverage. Note that in contrast to equation (1b), equation (1a) requires no assumption about the reaction kinetics and, hence, in the following, it is used for analysis.

In pulse-mode operation,  $\tau_{1/2}$  scales with the laser pulse length  $\tau_{1/2} \propto \tau$  [54].  $T$ , in turn, is calculated on the basis of an analytical solution of the corresponding heat conduction equation [41, 81, 82]. In particular, as constant temperatures are established on a nanosecond time scale [50], stationary temperature profiles are considered. Also, at a penetration depth of

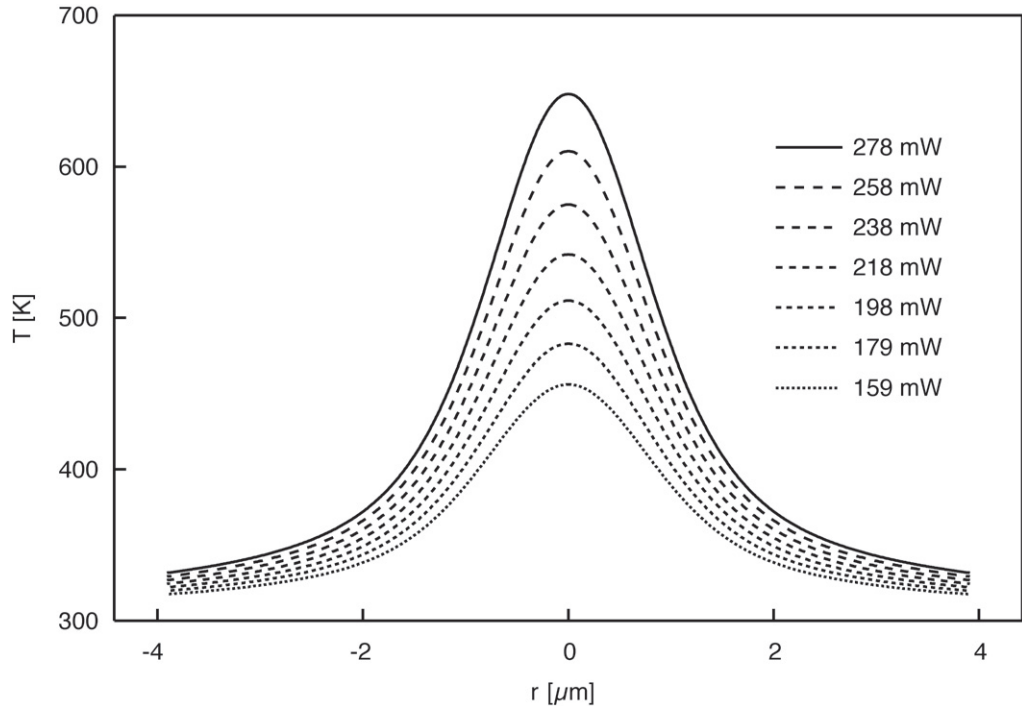


**Figure 12.** Stationary temperature profiles at the incident laser powers  $P$  in the patterning experiments of this study, cf figure 10(a). Temperature profiles are calculated on the basis of equations (2a) and (2b) with  $T_0 = 300$  K,  $T_k = 96$  K,  $d_{1/e^2} = 2.8$   $\mu\text{m}$ ,  $\kappa = 1.48$   $\text{W cm}^{-1} \text{K}^{-1}$  and  $R = 0.62$ .

22 nm [75], laser absorption is essentially limited to the thin Au film, whereas heat conduction is dominated by the underlying silicon substrate [55]. Hence, the radial variation of the temperature  $T$  at the surface is given by [41, 50]:

$$T = T_k + (T_0 - T_k) \exp\left(\frac{\Delta T}{T_0 - T_k}\right), \quad (2a)$$

with

$$\Delta T = \frac{\sqrt{2/\pi} P (1 - R)}{\kappa d_{1/e^2}} I_0\left(\left(\frac{2r}{d_{1/e^2}}\right)^2\right) \exp\left(-\left(\frac{2r}{d_{1/e^2}}\right)^2\right), \quad (2b)$$

where  $r$  corresponds to the radial position relative to the center of the laser spot,  $\Delta T$  represents the linearized temperature rise,  $T_0 = 300$  K is the basic sample temperature,  $\kappa = 1.48$   $\text{W cm}^{-1} \text{K}^{-1}$  denotes the thermal conductivity at room temperature and  $T_k = 96$  K is a parameter that is commonly used to fit the temperature dependence of the thermal conductivity of silicon [41].  $I_0$  is the modified Bessel function of order zero,  $P$  is the incident laser power and  $R$ , here, corresponds to the measured reflectivity of the Au-coated substrates, which is  $R = 0.62$ .

Figure 12 shows the calculated temperature profiles for the incident laser powers in this study. Although these temperature calculations consider certain approximations [50, 55], equations (2a) and (2b) generally provide good estimates of the actual temperature profiles

on silicon-based platforms [41, 50, 54, 62]. As evident from figure 12, peak temperatures are between 450 and 650 K, which is known to facilitate desorption of thiol molecules [83]–[86].

Considering the laser pulse lengths  $\tau$  and the temperature calculations in figure 12, the data in figure 10(a) are plotted in an Arrhenius-type diagram on the basis of equation (1a), cf figure 11(b). A linear fit yields  $A = 10^{-18.2 \pm 1.4} \text{ s}$  and an activation energy  $E_A = 145 \pm 10 \text{ kJ mol}^{-1}$ , respectively. Note that, with increasing laser power, the individual data sets are slightly shifted toward higher temperatures, which is attributed to the temperature-dependent optical and thermal parameters that are not fully accounted for in the temperature calculations [41]. Note also that the error limits here reflect the statistical spread of the data. Additional uncertainties arise from experimental errors of the laser power and the laser spot diameter measurements.

### 3.3. Discussion and comparison

Overall, the values of  $E_A$  and  $A$  are in reasonable agreement with various results from studies focusing on the thermal desorption kinetics of alkanethiols on Au surfaces [83]–[86]. Generally, thermal desorption of long-chain alkanethiols from gold is described as a two-step mechanism. Kondoh *et al* [84] provided a detailed investigation of the adsorption and desorption of hexanethiol on Au(111) using thermal desorption spectroscopy and scanning tunneling microscopy. At high coverages,  $> 0.4 \text{ ML}$ , a densely packed phase is formed, in which the thiol molecules stand up on top of the surface. Desorption from this phase takes place via a bimolecular reaction, i.e. via disulfide formation. The respective kinetic parameters are  $\nu = 10^{-1 \pm 1} \text{ cm}^2 \text{ s}^{-1}$  and  $E_A = 126 \pm 8 \text{ kJ mol}^{-1}$ . At low coverages,  $< 0.4 \text{ ML}$ , a striped phase is formed, in which the thiol molecules adopt a flat-lying configuration. Molecules from this phase desorb as thiolate radicals following a unimolecular reaction with kinetic parameters of  $\nu = 10^{17 \pm 2} \text{ s}^{-1}$  and  $E_A = 167 \pm 21 \text{ kJ mol}^{-1}$ . In the experiments described here, it is expected that etching sets in at high coverages, i.e. at  $> 0.4 \text{ ML}$ . Hence, the size of the final structures should be determined by the high-coverage desorption kinetics. Considering the overall error, however, the activation energy of  $E_A = 145 \pm 10 \text{ kJ mol}^{-1}$ , is clearly close to both the high and low coverage parameters. Similarly, there is reasonable agreement with the prefactor of  $A = 10^{-18.2 \pm 1.4} \text{ s}$ . In particular, considering an initial surface coverage of  $\theta_0 = 4.6 \times 10^{14} \text{ cm}^{-2}$  [84], frequency factors of  $\nu = 10^{18.1 \pm 1.2} \text{ s}^{-1}$  and  $\nu = 10^{3.5 \pm 1.4} \text{ s}^{-1}$ , respectively, are calculated for a first-order and a second-order reaction. It is also worth noting that rapid laser-induced desorption in many cases opens up new reaction channels [77]–[79]. In particular, the patterning process in the experiments described here could well follow a different kinetics than observed in standard thermal desorption studies [83]–[86].

In view of the results from the thermokinetic analysis, the highly nonlinear dependence of the overall patterning process on the laser intensity is attributed to the high activation energy for thermal desorption of the thiol molecules. It is illustrative to compare the laser intensity profile and the corresponding temperature profile with the lateral variation of the reaction rate constant and the surface coverage of the thiol molecules. For simplicity, scaled profiles are shown in figure 13. The scaled laser intensity profile  $I^*$  is simply calculated using the experimentally determined  $1/e^2$  laser spot diameter  $d_{1/e^2}$ :

$$I^* = I/I_{\max} = \exp\left(-d_{1/e^2}^2/2r^2\right). \quad (3a)$$

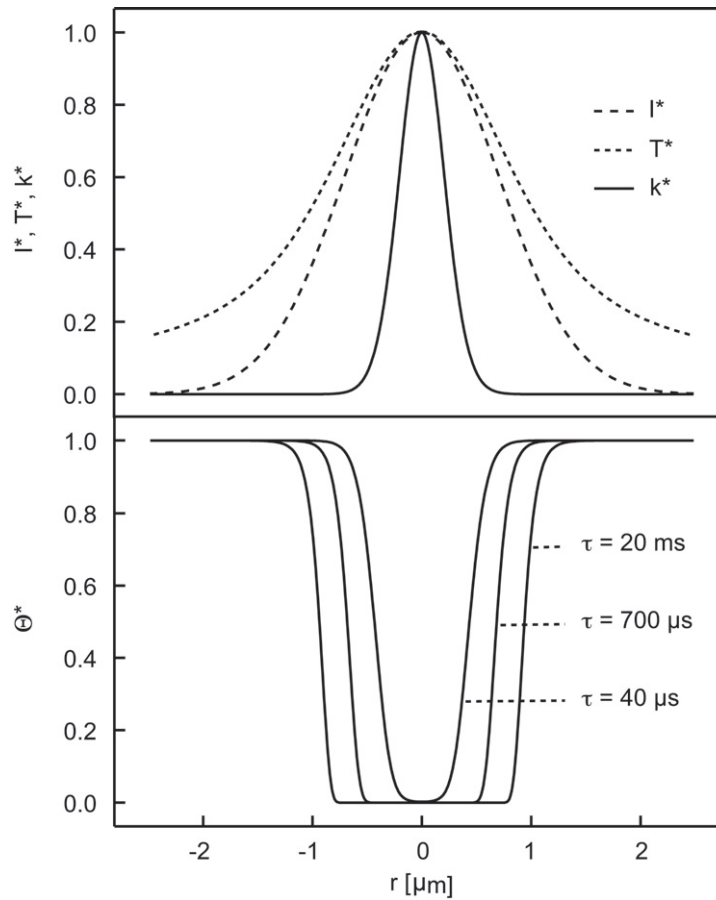


**Figure 13.** Scaled profiles of the laser intensity  $I^*$ , the surface temperature  $T^*$ , the reaction rate constant  $k^*$  and the surface coverage  $\theta^*$  at distinct laser pulse lengths  $\tau$ . Profiles are calculated on the basis of equations (1b), (2a), (2b) and (3a)–(3d) with  $T_0 = 300$  K,  $T_k = 96$  K,  $d_{1/e^2} = 2.8$   $\mu\text{m}$ ,  $\kappa = 1.48$   $\text{W cm}^{-1} \text{K}^{-1}$ ,  $P = 238$  mW and  $R = 0.62$  and the kinetic parameters from the thermokinetic analysis:  $A = 10^{-18.2}$  s and  $E_A = 145$   $\text{kJ mol}^{-1}$ .

The scaled temperature profile  $T^*$ , in turn, is calculated from equations (2a) and (2b) via:

$$T^* = \frac{T - T_0}{T_{\max} - T_0}. \quad (3b)$$

Finally, the scaled profile of the reaction rate constant  $k^*$  and the scaled surface coverage profile  $\theta^*$ , respectively, are calculated from equation (1b) assuming a first-order reaction via

$$k^* = \frac{k - k_0}{k_{\max} - k_0}, \quad (3c)$$

and

$$\theta^* = \theta / \theta_{\text{sat}} = \exp(-k\tau), \quad (3d)$$

where  $k_0$  in (3c) represents the rate constant at the basic sample temperature  $T_0$ ;  $I_{\max}$ ,  $T_{\max}$ ,  $k_{\max}$  and  $\theta_{\text{sat}}$  in (3a)–(3d) represent the peak intensity, peak temperature, peak rate constant and saturation coverage, respectively.

**Table 1.** Prefactors  $A$  and activation energies  $E_A$  from a thermokinetic analysis of data from patterning experiments of distinct types of organic monolayers.

Precursor(s)	Substrate(s)	$A$ (s)	$E_A$ (kJ mol <sup>-1</sup> )	Reference
Octadecyltrichlorosilane	SiO <sub>2</sub> /Si(100)	10 <sup>-18.1±0.7</sup>	425 ± 25	[50]
Hexadecene, -decyne	Si(100), Si(111)	10 <sup>-15.1±2.1</sup>	282 ± 29	[54]
Hexadecanethiol	Au/SiO <sub>2</sub> /Si(100)	10 <sup>-18.2±1.4</sup>	145 ± 10	This work

As shown in figure 13, at a given laser power, the width of the structures decreases with decreasing laser pulse length. At short pulse length, desorption of the thiol molecules remains confined to the center of the laser spot where high temperatures and reaction rates are reached. Similarly, with decreasing laser power, the width of the structures decreases because of the reduced width of the temperature profiles as displayed in figure 12.

For comparison, table 1 displays the kinetic parameters for distinct types of SAMs. All these parameters have been obtained via thermokinetic analysis of data from patterning experiments with an Ar<sup>+</sup> laser using the same experimental setup. The activation energies nicely reflect the general order of these SAMs in terms of thermal and chemical stability [28]–[30]. It is worth noting that, despite a comparatively low activation energy, photothermal laser patterning of HDT SAMs, as reported here, yields fairly small structures. In particular, at a  $1/e^2$  laser spot diameter of 2.8  $\mu\text{m}$ , minimum structure sizes are close to 250 nm. This approaches the lateral dimensions of 200 nm obtained in photothermal patterning of alkylsiloxane monolayers [50]. Future studies will show whether this high resolution can also be exploited to build up nanostructured chemical templates via backfilling of the laser-depleted areas with functional thiol molecules [55, 57].

#### 4. Conclusions and perspectives

In conclusion, photothermal patterning of HDT monolayers on Au-coated silicon samples with sub-wavelength resolution has been demonstrated using a focused beam of an Ar<sup>+</sup> laser at  $\lambda = 514$  nm. In particular, the minimum structure sizes, at a  $1/e^2$  laser spot diameter of 2.8  $\mu\text{m}$ , are close to 250 nm. Fabrication of smaller structures requires tighter focused laser beams. Considering high-aperture optics and/or shorter wavelengths,  $1/e^2$  laser spot sizes down to 500 nm and below can be reached [58]. Hence, fabrication of structures with lateral dimensions below 100 nm appears feasible. Future studies, of course, have to show to what extent thermal transport mechanisms on the nanoscale limit the fabrication of smaller structures. Also, photochemical reactions might dominate processing at wavelengths in the deep UV region [28, 74]. In both respects, common near-infrared femtosecond lasers offer promising perspectives in photothermal processing.

In addition to its unexpectedly high lateral resolution, the procedure provides a powerful combination of other features, i.e. it is based on a noncontact maskless process and allows for rapid patterning in ambient conditions. It is also anticipated that continuing progress in laser and display technology will soon allow this approach to be exploited as a truly cost-effective parallel means, e.g. using digital mirror displays and micro-lens arrays. In view of these results and perspectives, photothermal laser processing constitutes a powerful tool for large-area

micro- and nanopatterning of thiol-type SAMs. Future studies will take particular advantage of such photothermal routines to build up thiol-based chemical templates.

On a broader view, the results reported here nicely complement our previous studies in this field demonstrating the overall versatility of nonlinear laser processing in sub-wavelength patterning of self-assembled organic monolayers on metallic, semiconducting and dielectric platforms [45], [50]–[54], [59]–[63]. In addition to photothermal processing with continuous-wave lasers [51]–[54], [59]–[63], femtosecond lasers provide unique opportunities in nonlinear processing of organic monolayers via multiphoton absorption processes [45]. In particular, work in progress addresses the fabrication of 3D chemical templates on the basis of silica aerogels [87].

## Acknowledgments

Financial support from the Deutsche Forschungsgemeinschaft (DFG; grant HA-2769/3–1), the BASF Coatings AG and the European Union and the Ministry of Economic Affairs and Energy of the State North Rhine-Westphalia in Germany (Objective 2 Programme: European Regional Development Fund, ERDF) is gratefully acknowledged. NH also thanks Eckart Hasselbrink for his continuous support.

## References

- [1] Xia Y, Rogers J A, Paul K E and Whitesides G M 1999 *Chem. Rev.* **99** 1823
- [2] Gates B D, Xu Q, Stewart M, Ryan D, Willson C G and Whitesides G M 2005 *Chem. Rev.* **105** 1171
- [3] Geissler M and Xia Y 2004 *Adv. Mater.* **16** 1249
- [4] Prinz A A and Fromherz P 2000 *Biol. Cybern.* **82** L1
- [5] Willner I and Katz E (ed) 2005 *Bioelectronics: From Theory to Applications* (Weinheim: Wiley-VCH)
- [6] Kramper P, Birner A, Agio M, Soukoulis C M, Müller F, Gösele U, Mlynek J and Sandoghdar V 2001 *Phys. Rev. B* **64** 233102
- [7] Pavesi L and Lockwood D J 2004 *Silicon Photonics* (Berlin: Springer)
- [8] Rai-Choudhury P (ed) 1997 *Handbook of Microlithography, Micromachining, and Microfabrication* vols 1 and 2 (Bellingham, WA: SPIE Optical Engineering Press)
- [9] Sotomayor Torres C M 2003 *Alternative Lithography* (New York: Kluwer/Plenum)
- [10] Madou M 2002 *Fundamentals of Microfabrication: The Science of Miniaturization* (Boca Raton, FL: CRC Press)
- [11] Steed J W and Atwood J L 2000 *Supramolecular Chemistry* (Chichester: Wiley)
- [12] Hadjichristidis N, Pispas A and Floudas G 2003 *Block Copolymers: Synthetic Strategies, Physical Properties, and Applications* (Hoboken: Wiley)
- [13] Schmid G 2004 *Nanoparticles: From Theory to Application* (Weinheim: Wiley-VCH)
- [14] Nyffenegger R M and Penner R M 1997 *Chem. Rev.* **97** 1195
- [15] Wouters D and Schubert U S 2004 *Angew. Chem., Int. Ed. Engl.* **43** 2480
- [16] Flink S, van Veggel F C J M and Reinhoudt D N 2000 *Adv. Mater.* **12** 1315
- [17] Park C, Yoon J and Thomas E L 2003 *Polymer* **44** 6725
- [18] Shipway A N, Katz E and Willner I 2000 *ChemPhysChem* **1** 18
- [19] Woodson M and Liu J 2007 *Phys. Chem. Chem. Phys.* **9** 207
- [20] Mendes P M and Preece J A 2004 *Curr. Opin. Colloid Interface Sci.* **9** 236
- [21] Segalman R A 2005 *Mat. Sci. Eng. R* **48** 191
- [22] Xia Y, Yin Y, Lu Y and McLellan J 2003 *Adv. Funct. Mater.* **13** 907

- [23] Dziomkina N V and Vancso G J 2005 *Soft Matter* **1** 265
- [24] Quinn J F, Johnston A P R, Such G K, Zelkin A N and Caruso F 2007 *Chem. Soc. Rev.* **36** 707
- [25] Ariga K, Hill J P and Ji Q 2007 *Phys. Chem. Chem. Phys.* **9** 2319
- [26] Wang Y, Angelatos A S and Caruso F 2008 *Chem. Mater.* **20** 848
- [27] Schreiber F 2000 *Prog. Surf. Sci.* **65** 151
- [28] Love J C, Estroff L A, Kriebel J K, Nuzzo R G and Whitesides G M 2005 *Chem. Rev.* **105** 1103
- [29] Onclin S, Ravoo B J and Reinhoudt D N 2005 *Angew. Chem., Int. Ed. Engl.* **44** 6282
- [30] Buriak J M 2002 *Chem. Rev.* **102** 1271
- [31] Smith R K, Lewis P A and Weiss P S 2004 *Prog. Surf. Sci.* **75** 1
- [32] Sullivan T P and Huck W T S 2003 *Eur. J. Org. Chem.* 17
- [33] Schreiber F 2004 *J. Phys.: Condens. Mater.* **16** R881
- [34] Xia Y and Whitesides G M 1998 *Angew. Chem., Int. Ed. Engl.* **37** 550
- [35] Zharnikov M and Grunze M 2002 *J. Vac. Sci. Technol. B* **20** 1793
- [36] Liu G Y, Xu A and Qian Y 2000 *Acc. Chem. Res.* **33** 457
- [37] Wouters D, Hoepfner S and Schubert U S 2009 *Angew. Chem., Int. Ed. Engl.* **48** 1732
- [38] Leggett G J 2006 *Chem. Soc. Rev.* **35** 1150
- [39] Ginger D S, Zhang H and Mirkin C A 2004 *Angew. Chem., Int. Ed. Engl.* **43** 30
- [40] Roy S 2007 *J. Phys. D: Appl. Phys.* **40** R413
- [41] Bäuerle D 2000 *Laser Processing and Chemistry* (Berlin: Springer)
- [42] Ali M, Wagner T, Shakoor M and Molian P A J 2008 *Laser Appl.* **20** 169
- [43] Chong T C, Hong M H and Shi L P 2010 *Laser Photonics Rev.* **4** 123
- [44] Koch J, Korte F, Fallnich C, Ostendorf A and Chichkov B N 2005 *Opt. Eng.* **44** 051103
- [45] Hartmann N, Franzka S, Koch J, Ostendorf A and Chichkov B N 2008 *Appl. Phys. Lett.* **92** 223111
- [46] Álvarez M, Best A, Pradhan-Kadam S, Koynov K, Jonas U and Kreiter M 2008 *Adv. Mater.* **20** 4563
- [47] Chang W, Choi M, Kim J, Cho S and Whang K 2005 *Appl. Surf. Sci.* **240** 296
- [48] Chang W, Kim J, Cho S and Whang K 2006 *Japan. J. Appl. Phys.* **45** 2082
- [49] Kirkwood S E, Shadnam M R, Amirfazli A and Fedosejevs R 2007 *J. Phys. Conf. Ser.* **59** 428
- [50] Balgar T, Franzka S and Hartmann N 2006 *Appl. Phys. A* **82** 689
- [51] Hartmann N, Balgar T, Bautista R and Franzka S 2006 *Surf. Sci.* **600** 4034
- [52] Dahlhaus D, Franzka S, Hasselbrink E and Hartmann N 2006 *Nano Lett.* **6** 2358
- [53] Mathieu M, Friebe A, Franzka S, Ulbricht M and Hartmann N 2009 *Langmuir* **25** 12393
- [54] Klingebiel B, Scheres L, Franzka S, Zuilhof H and Hartmann N 2010 *Langmuir* **26** 6826
- [55] Shadnam M R, Kirkwood S E, Fedosejevs R and Amirfazli A 2004 *Langmuir* **20** 2667
- [56] Shadnam M R, Kirkwood S E, Fedosejevs R and Amirfazli A 2005 *J. Phys. Chem. B* **109** 11996
- [57] Rhinow D and Hampp N A 2007 *Adv. Mater.* **19** 1967
- [58] Iversen L, Younes-Metzler O, Martinez K L and Stamou D 2009 *Langmuir* **25** 12819
- [59] Mathieu M, Schunk D, Franzka S, Mayer C, Hasselbrink E and Hartmann N 2009 *Small* **5** 2099
- [60] Balgar T, Franzka S, Hartmann N and Hasselbrink E 2004 *Langmuir* **20** 3525
- [61] Balgar T, Franzka S, Hasselbrink E and Hartmann N 2006 *Appl. Phys. A* **82** 15
- [62] Hartmann N, Klingebiel B, Balgar T, Franzka S and Hasselbrink E 2009 *Appl. Phys. A* **94** 95
- [63] Klingebiel B, Schröter A, Franzka S and Hartmann N 2009 *ChemPhysChem* **10** 2000
- [64] Zhang F *et al* 2006 *Langmuir* **22** 10859
- [65] Koch J, Fadeeva E, Engelbrecht M, Ruffert C, Gatzel H H, Ostendorf A and Chichkov B N 2006 *Appl. Phys. A* **82** 23
- [66] Misawa H and Juodkazy S 2006 *3D Laser Microfabrication* (Weinheim: Wiley-VCH)
- [67] Bäuerle D 2008 *Grundlagen und Anwendungen in Photonik, Technik, Medizin und Kunst* (Berlin: Wiley-VCH)
- [68] Zhou X L, Zhu X Y and White J M 1991 *Surf. Sci. Rep.* **13** 73
- [69] Richter L J and Cavanagh R R 1992 *Prog. Surf. Sci.* **39** 155

- [70] Zimmermann F M and Ho W 1995 *Surf. Sci. Rep.* **22** 127
- [71] Zhang F, Gates R J, Smentkowski V S, Natarajan S, Gale B K, Watt R K, Asplund M C and Linford M R 2007 *J. Am. Chem. Soc.* **129** 9252
- [72] Geldhauser T, Leiderer P, Boneberg J, Walheim S and Schimmel T 2008 *Langmuir* **24** 13155
- [73] Xia Y, Zhao X M, Kim E and Whitesides G M 1995 *Chem. Mater.* **7** 2332
- [74] Ryan D, Parviz B A, Linder V, Semetey V, Sia S K, Su J, Mrksich M and Whitesides G M 2004 *Langmuir* **20** 9080
- [75] Lide D R 2009 *CRC Handbook of Chemistry and Physics* (London: Taylor and Francis)
- [76] Burgess D, Stair P C and Weitz E 1986 *J. Vac. Sci. Technol. A* **4** 1362
- [77] Ertl G and Neumann M 1972 *Z. Naturforsch. A* **27a** 1607
- [78] Hall R B 1987 *J. Phys. Chem.* **91** 1007
- [79] Dürr M, Biedermann A, Hu Z, Höfer U and Heinz T F 2002 *Science* **296** 1838
- [80] Pilling M J and Seakins P W 1999 *Reaction Kinetics* (Oxford: Oxford University Press)
- [81] Ehrlich D J and Tsao J Y (ed) 1989 *Laser Microfabrication* (Boston, MA: Academic)
- [82] Poate J M and Mayer J W (ed) 1982 *Laser Annealing of Semiconductors* (New York: Academic)
- [83] Nishida N, Hara M, Sasabe H and Knoll W 1996 *Japan J. Appl. Phys.* **35** 5866
- [84] Kondoh H, Kodama C, Sumida H and Nozoye H 1999 *J. Chem. Phys.* **111** 1175
- [85] Rading D, Kerstin R and Benninghoven A 2000 *J. Vac. Sci. Technol. A* **18** 12
- [86] Shadnam M R and Amirfazli A 2005 *Chem. Commun.* 4869
- [87] Sutapa G, Baumann T F, King J S, Kucheyev S O, Wang Y, Worsley M A, Biener J, Bent S F and Hamza A V 2009 *Chem. Mater.* **21** 1989